P3HT:PCBM polymer solar cells from a didactic perspective

Shahidul Alam,[a,*] **Aman Anand**,[b,c] **Md Moidul Islam**,[b,c]
Rico Meitzner,[b,c] **Aurelien Sokeng Djoumessi**,[b,c] **Josef Slowik**,[b,c]
Zekarias Teklu,[b,c] **Peter Fischer**,[d] **Christian Kästner**,[e] **Jafar I. Khan**,[a]
Ulrich S. Schubert,[b,c] **Frédéric Laquai**,[a] **and Harald Hoppe**[b,c]
[a]King Abdullah University of Science and Technology, KAUST Solar Center, Physical Sciences and Engineering Division, Thuwal, Saudi Arabia
[b]Friedrich Schiller University Jena, Laboratory of Organic and Macromolecular Chemistry, Jena, Germany
[c]Friedrich Schiller University Jena, Center for Energy and Environmental Chemistry Jena, Jena, Germany
[d]Ilmenau University of Technology, Institute of Materials Engineering, Ilmenau, Germany
[e]Technische Universität Ilmenau, Production Technology Group, Ilmenau, Germany

Abstract. Here, we studied the influence of pre- and post-thermal annealing on the performance of polymer:fullerene bulk heterojunction solar cells using the conventional architecture, comprising a conjugated polymer, namely, poly(3-hexylthiophene-2,5-diyl) (P3HT) and a fullerene derivative [6,6]-phenyl-C60-butyric acid methyl ester ($PC_{60}BM$) as a photoactive layer. The non-annealed active layer device exhibited a power conversion efficiency of <1%, which was significantly lower than the pre- and post-annealed devices. To investigate the impact of pre- and post thermal annealing on the natural morphological state of the polymer, regiorandom (P3HT-I) and regioregular (P3HT-II) type P3HT were compared in photoactive layers. In general, P3HT-I is amorphous, whereas P3HT-II is semi-crystalline. Changes in solar cell performance were associated with changes in carrier extraction efficiencies influenced by the annealing conditions. The charge photogeneration processes were investigated using spectroscopic techniques, including electroluminescence, steady-state, and time-resolved photoluminescence spectroscopy. Finally, to explore the morphological changes upon annealing, atomic force microscopy and electroluminescence imaging measurements were performed on films and solar cells, respectively. [DOI: 10.1117/1.JPE.12.035501]

Keywords: bulk-heterojunction polymer solar cells; poly(3-hexylthiophene): [6,6]-phenyl-C61-butyric acid methyl ester solar cells; thermal annealing; pre-and post-annealing.

Paper 22019G received Mar. 27, 2022; accepted for publication Aug. 2, 2022; published online Aug. 23, 2022.

1 Introduction

With the latest prominent rise in the development of organic solar cells (OSCs), there is a continuous influx of interested students in the OSC research and development field.[1] Lately, researchers have been fascinated mainly by novel non-fullerene acceptors (NFAs) combined with high-performing mid-bandgap polymers.[2,3] However, poly(3-hexylthiophene) (P3HT) and 1-(3-methoxycarbonyl)propyl-1-phenyl[6,6]C61 (PCBM) blend is one of the most-studied photoactive layers in OSCs.[4–9] According to Wantz et al.,[10] a remarkable number of papers were published between 2002 and 2010. After a decade, there is still interest in P3HT:PCBM-based devices due to their novel properties and useful aspects compared to NFA-based solar cells.[11–13] Due to the polymers versatile properties, many organic materials have been developed for photovoltaic applications over the last 20 years of applications.[14–17] With the development of novel NFAs that match well with the old P3HT, efficiencies in the range of 10% and beyond are within

---

*Address all correspondence to Shahidul Alam, shahidul.alam@kaust.edu.sa

sight. One of the greatest benefits that P3HT offers over the novel mid-bandgap polymers is that it can be synthesized with a high yield at relatively low costs. Generally speaking, the more complex the synthesis, the higher the associated costs, making it very hard to reach the same economics as with P3HT production.[18] In addition, NFAs that are tailor-made for P3HT nicely complement its limited absorption range and may thus be the perfect partner for P3HT. Moreover, there is still ongoing research for materials that can boost P3HT-based OSCs over the 10% efficiency limit. Despite significant advancements concerning OSC power conversion efficiency (PCE) over the past decade, there is still an ongoing debate over the physical processes restraining the device performance.[19,20]

The crystallinity of P3HT has been shown to play a critical role in the PCE of OSC devices due to its relationship to charge carrier mobility and percolation pathways. Furthermore, to improve the crystallinity of the P3HT in OSC to increase the charge carrier mobility and PCE, several approaches such as additives and solvent blends, thermal and vapor annealing, or combinations have been carried out.[21–26] There are two significant considerations for arranging donor and acceptor phases in the concept of bulk-heterojunction (BHJ) polymer solar cell design. First, the homogeneous mixture of the donor and acceptor phase in the photoactive layer allows for a large interfacial area, which leads to efficient exciton dissociation.[27–31] Second, establishing an interpenetrating, semi-crystalline donor–acceptor network for charge transport.[32–34] Since as-cast or non-annealed P3HT:PCBM films are mostly amorphous in structure, this unordered structure severely limits the conduction and charge carrier mobility.[35,36] As a result, the devices often show low-charge carrier mobility and, ultimately, low-charge carrier photocurrent and fill factors.[37–39] The main idea behind the annealing step is to change the active layer morphology from homogeneously intermixed amorphous to a more phase-separated semi-crystalline structure.[37,40,41] The films undergo this transition due to an alignment of the polymer chains to form crystallites.[42] For higher annealing temperatures, the PCBM phases are further phase separated by induced aggregation.[43] This aggregation may reduce the exciton dissociation rate by decreasing the interfacial area.[44] The thermal annealing parameters of both temperature and time vastly affect the rate at which this transition occurs.[45,46] Some non-obvious optimum conditions provide the most favorable exciton dissociation and charge percolation.[42,47]

The main focus of this study is to investigate the properties of P3HT:PCBM-based solar cells and to understand the effect of thermal annealing on the performance of the device prepared in the conventional architecture. In particular, we examine the changes in the physical properties of the active layer, the electronic characteristics of the solar cells, and the relationship between morphology and electronic performance upon the annealing process.[48,49] To elucidate the impact of boundary conditions of P3HT:PCBM solar cells, two types of P3HT (regiorandom and regioregular) were used to prepare the devices, and those were annealed before and after electrode deposition and compared with as-cast/non-annealed devices. It was observed that the thermal annealing of devices leads to an increase in the conjugation length of P3HT, leading to phase separation of P3HT and PCBM and ultimately increasing the PCE by ~350% for amorphous and ~900% for semi-crystalline P3HT. However, annealing conditions (pre and post) have a significant impact on the performance of OSCs. Hence, we report the changes induced by thermal annealing under different conditions, and the effect of the annealing sequence of the solar cell devices was investigated by several optoelectrical characterization techniques. Photoluminescence (PL) quenching and lifetimes were analyzed by using steady-state (SS), and time-resolved photoluminescence (TRPL) spectroscopy and are consistent with P3HT-II-based blend yielding complete PL quench (93%) compared to non-annealed P3HT-I (26%)-based blend. Atomic force microscopy (AFM) and electroluminescence imaging (ELI) were carried out for an in-depth analysis of morphological changes upon annealing of P3HT:PCBM blend films and solar cell devices, respectively.

2 Experimental Section

2.1 *Materials*

Two different types of commercial P3HT samples were acquired from 1-M (P3HT-I) and BASF P200 (P3HT-II). These two commercial P3HTs were chosen to study based on the viability of these materials available from suppliers that are most commonly used in the labs within the organic photovoltaics community. As an acceptor material, $PC_{60}BM$ was used supplied by Solene. To facilitate the charge transport, PEDOT:PSS (P VP AI 4083) was used as a hole transport layer received from Clevios. Whatman polyethersulfone 0.45-μm filters were used to deposit PEDOT:PSS on pre-structured indium tin oxide (ITO) received from Xinyan Technology Limited.

2.2 *Solar Cell and Thin-Film Fabrication*

BHJ polymer solar cells were fabricated with conventional architecture. ITO-coated glasses were first cleaned with acetone and isopropanol for 15 min consecutively in an ultrasonic bath to fabricate conventional structured solar cells. PEDOT:PSS solution, filtered with 0.45-μm filter, was spun-cast at 3000 rpm for 60 s and thermally annealed at 178°C for 15 min in the air to remove residual water. The concentration of the $\mathrm{P3HT:PC_{60}BM}$ (composition weight ratio-3:2) solution was 12 mg/ml, dissolved in chlorobenzene anhydrous (from Sigma Aldrich). The solution was spin-coated on the PEDOT:PSS layer at 750 rpm for 60 s, inside the glovebox. The solution was held at 50°C during the coating process. After processing the active layer, the samples were placed into a vapor deposition chamber. About 200-nm thick layer of aluminum (Al) was thermally deposited as an electrode in ultra-high vacuum through a shadow mask. The devices were sealed with glass using UV-curing adhesive (received from DELO).

To study the effect of thermal annealing at a different step of processing, the devices were thermally annealed at 150°C for 10 min under two conditions: (i) pre-annealed; partially completed device up to the active layer; and (ii) post-annealed, completed device after metal deposition. To do the optical and morphological characterizations, P3HT:PCBM films were prepared on glass slides just as the active layer of the solar cells, i.e., the glass slides were cleaned with acetone and isopropanol for 15 min consecutively in an ultrasonic bath and P3HT:PCBM films were spun-cast at 750 rpm for 60 s. Two substrates were prepared, one was left untreated as a reference, and the others were annealed at 160°C for 5 min.

2.3 *Solar Cell and Thin-Film Characterization*

External quantum efficiency (EQE): The EQE were recorded with a Bentham PVE300 photovoltaic characterization system under monochromatic light and additional halogen bias light, providing an excitation intensity of about one sun. A Si detector was used to calibrate the system.

Current–voltage (I–V) measurements: The I–V curves were acquired in the dark and under the illumination of one sun (AM 1.5) solar simulator and were recorded with a Keithley 2400 source-meter-unit (SMU). The intensity of the light source was calibrated by standard silicon (Si) photodiode to confirm the AM1.5 condition and the intensity of $100\ \mathrm{mW/cm^2}$.

Absorption and PL: Contactless and non-destructive thin film steady-state photoluminescence (SSPL) spectra were recorded with an AvantesAvaSpec ULS-2048 fiber spectrometer, with an integration time of 5 s. PL excitation was conducted with a laser diode emitting at 405 nm. For PL correction by absorption and evaluation of optical bandgaps, thin-film transmission and reflection spectra were simultaneously recorded with two Avantes AvaSpec-ULS3648-USB2-UA-25 fiber spectrometers and reassembled to the thin film absorption spectra.

Electroluminescence (EL): EL spectra were recorded in a home-built setup with an AvaSpec ULS-2048 fiber spectrometer. A Keithley 2601 SMU was used for electrical excitation of the samples with a 200-mA injection current under forward bias, with an integration time of 5 s.

TRPL: The measurements were performed using 450-nm excitation from Coherent (Chameleon) fs laser operating at 80-MHz repetition rate. The thin films were kept in a small nitrogen-filled chamber, and the fluences were in order of $600\ \mathrm{nJ/cm^2}$. The PL of the samples was collected by an optical telescope (consisting of two plano-convex lenses) and focused on the slit of a spectrograph (PI Spectra Pro SP2300) and detected with a Streak Camera (Hamamatsu C10910) system with a temporal resolution of 1.4 ps. The data were acquired in photon counting mode using the Streak Camera software (HPDTA) and exported to Origin Pro 2020 for further analysis.

AFM: To gain further insight into the morphology of the blend systems, AFM measurements were performed in tapping mode on a NTEGRA Aura (NT-MDT) using tapping mode cantilevers from Mikromasch (NSC35). The images were analyzed by Gwyddion multiplatform modular free software.

ELI: To see the active layer inhomogeneity in the solar cells, ELI measurements were applied laterally to resolve the EL signal. ELI is very sensitive to changes and local modifications of the series resistance and the dark saturation current. To image the EL of the solar cells, they were placed in a multiple sample holder and individually measured with an automated program. Therefore, a constant current was applied with a Keithley 2400 SMU, and the emitted light was recorded with a cooled Si CCD camera. The applied current density was 200 mA/cm^2, and the signal was integrated for 10 s with two averages. The camera ANDOR iKon-M was cooled to −50°C for noise reduction.

3 Results and Discussion

In general, P3HT:PCBM blends exhibit a disordered morphology when spin-cast from solvents with relatively low boiling points as chloroform. This disordered morphology is detrimental for charge transport but can be overcome by annealing which improves the morphology by demixing and enhancing crystallization of P3HT and PCBM, beneficial for efficient charge carrier extraction. The moderate photocurrent is evident for as-cast or non-annealed devices with impeded charge transport properties, as revealed by the solar cells' current density–voltage (J–V) characteristics. The solar cells were prepared in conventional architecture with a layer stack of glass/ITO/photoactive layer/Al. The details of the solar cell preparation and step-by-step fabrication processes are shown in Fig. 8 in the Appendix. The chemical structures of regioregular and regiorandom P3HT and PC$_{60}$BM are shown in Fig. 1(a), and the schematic of

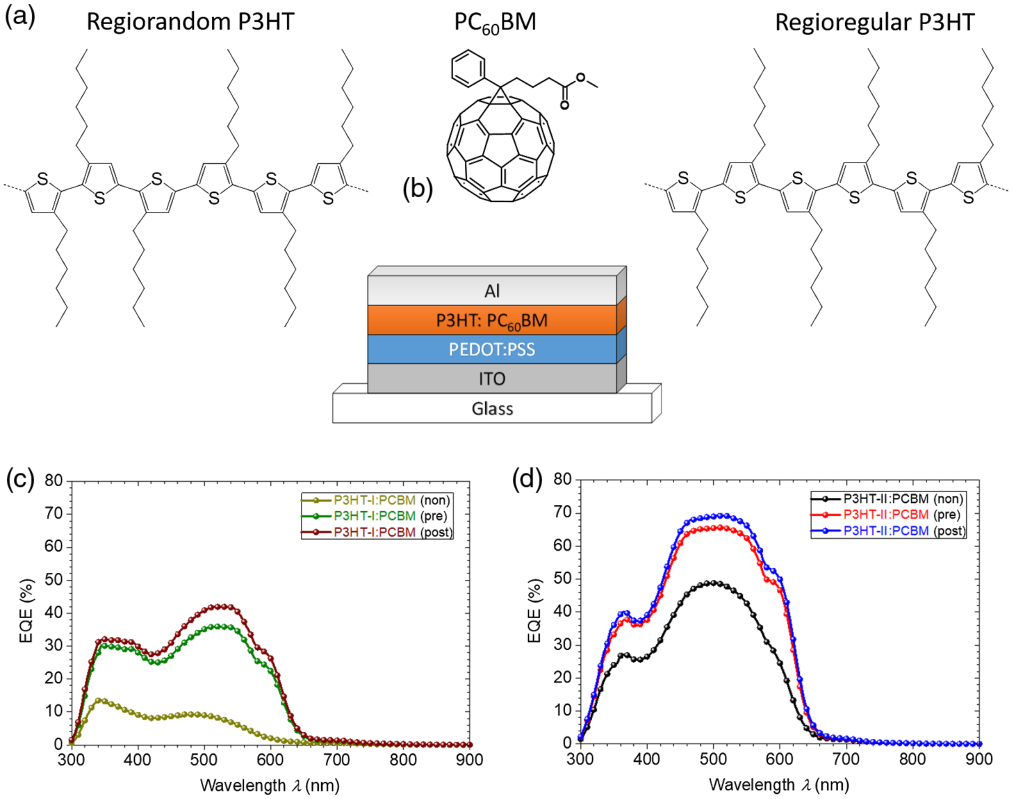

Fig. 1 (a) Chemical structure of regiorandom poly(3-hexylthiophene) (named P3HT-I), regioregular poly(3-hexylthiophene) (named P3HT-II) and PC$_{60}$BM. (b) Schematic of the layer stack in conventional architecture. (c) EQE of P3HT-I:PCBM and (d) EQE of P3HT-II:PCBM-based solar cells.

the layer stacks is shown in Fig. 1(b). The spectral responses of the solar cells obtained after annealing are shown in Figs. 1(c) and 1(d).

Device performance statistics were taken from *I*–*V* characteristics of 8 fabricated solar cells, shown in Fig. 9 in the Appendix and *J*–*V* curves for the best solar cells under illumination and dark are shown in Fig. 2. The *J*–*V* curves of the non-annealed solar cells under illumination indicate that the device has no apparent current saturation in the reverse current direction and not the expected exponential *J*–*V* (diode) characteristics in the forward direction. Furthermore, a weak *S*-shape is observed, indicating the presence of a counter diode caused by charge carrier accumulation and low carrier mobility. In other words, the formation of a space charge zone at the electrode hinders charge extraction; this can also be seen from the low open-circuit voltage (V_{OC}) for this device. The non-annealed devices for both types of P3HT show insufficient demixing and no consistent donor and acceptor percolation pathways through the photoactive layer. The pre-annealed device shows no such blocking behavior, and therefore, a likely much more favorable stratification within the active layer. In the case of post-annealing, the morphology is more favorable, as specified by the slightly increased short-circuit current (J_{SC}), though only marginally more significant as for the pre-annealed case, as they both reach similar values of photocurrent (see Fig. 10 in the Appendix).

A substantial difference between pre-and post-annealing is found for the V_{OC}. In fact, the voltage is increased by about 170 to 200 mV for post-annealed devices compared to pre-annealed devices. This reduced V_{OC} for the pre-annealed devices hints to an immensely increased dark saturation current. This could indicate a Schottky-like contact between the active layer and the electrode, which does not seem to be present in the case of the post-annealed device. Therefore, the larger roughness of the pre-annealed film might also increase the distance between regions where Al and the active layer are intermixed, creating a wider zone of heavy doping in the active layer, as the Al, with its more significant charge carrier density than PCBM, injects electrons into the PCBM, wherever the materials are interfacing each other. Thus the distance between the intermixed active layer and Al electrode is smaller, which might be due to the smaller crystallinity of non-annealed films generating a narrower doping profile, and hence, a narrower space charge region, consequently an improved contact. Furthermore, the interfacial energy between the active layer and aluminium electrode induces segregation of

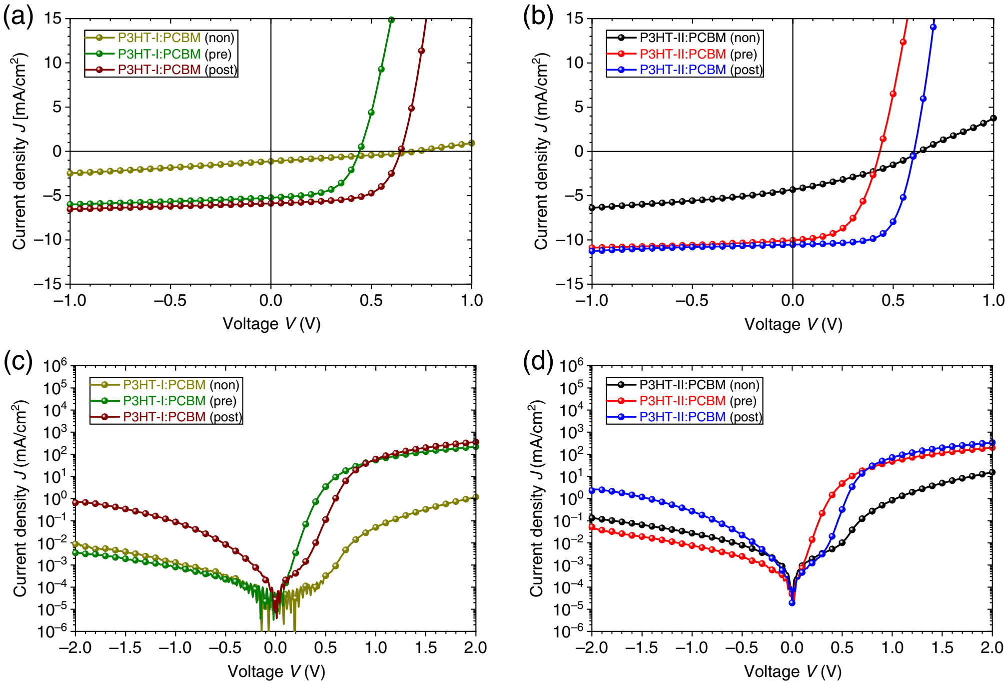

Fig. 2 Light and dark *I*–*V* characteristics of solar cells upon different annealing conditions. (a) P3HT-I:PCBM (sun); (b) P3HT-II:PCBM (sun); and (c) P3HT-I:PCBM (dark) and P3HT-II:PCBM (dark).

PCBM toward the anode, shifting the Fermi level of the electron extracting electrode, and additionally improving the electron extraction, signifying the slight increase of the photocurrent. In addition, the vertical phase segregation, i.e., counter-directed concentration gradients of donor and acceptor-rich domains between anode and cathode, further improves the charge percolation in both P3HT and PCBM. Thus, it can be concluded that a more favorable active layer morphology is formed and improves the charge carrier mobility upon annealing. The EQE spectra of the as-cast and annealed solar cells were measured to obtain the spectral response of the solar cells. It can be seen that a more pronounced shoulder around 600 nm is evident in thermally annealed devices, representing a higher crystallinity of the P3HT, consistent with the thermal treatment of both P3HT samples. Total current densities were calculated from the EQE spectra to correct the PCEs obtained from I–V measurements. The photovoltaic parameters of all solar cells and the corrected PCEs taking into account the current density calculated from EQE spectra are given in Table 1.

The dark J–V curves of all devices showed diode-like characteristics, while the non-annealed device showed somewhat lower rectification. Upon annealing, forward current densities increase by one order of magnitude. Though the forward current density increases for the pre-annealed device, only the post-annealed device shows decent diode characteristics. Remarkably, the pre-annealed samples exhibit a certain barrier for charge carrier injection. Interestingly, there are compelling trends in photovoltaic performances observed for the two different types of P3HT. The photocurrent for P3HT-II-based devices exhibited was almost twice the photocurrent of the P3HT-I-based devices. Furthermore, annealing increased J_{SC} and significantly improved the fill factor (FF). The non-annealed device that used P3HT-II exhibited poor device performance with $J_{\mathrm{SC}} = 4.31\ \mathrm{mA/cm^2}$ and $\mathrm{FF} = 34\%$, as evidenced by the almost linear J–V curve far from any ideal diode characteristics. The highest V_{OC} for non-annealed samples can be exhibited due to the quasi-fermi-level splitting at the contacts, the issue of the non-annealed solar cells show efficient charge generation, but with transport, which results in very high series resistance, as the current at V_{OC} is zero, this large series resistance does not effect the V_{OC}, but at non-zero current is quickly effects the device performance and results in an apparent lack of rectification as it massively limits the forward current. It can be seen that thermal treatment of the photoactive layers resulted in improved device performance of both aforementioned metrics. Thus, the crystallinity of the P3HT-II is enhanced, and the demixing of P3HT and PCBM is significantly enhanced for both types of P3HT compared to the non-annealed devices. This change in morphology is likely the reason for the dramatic reduction in series resistance (R_s). The R_s decreased by a factor of ∼50 for P3HT-I and a factor of about 7.5 for P3HT-II, when comparing the post-annealed samples to the non-annealed samples. The significant improvements can be attributed to the optimization of two crucial performance parameters, namely, the nanoscale crystallinity and phase segregation of the donor and acceptor phases. By looking at the R_P values of the solar cells, one can primarily conclude that the semi-crystalline P3HT (P3HT-II) materials show an increased dependence compared to the amorphous ones (P3HT-I).

Table 1 Photovoltaics parameters for the P3HT-(I&II):PCBM solar cells from IV-characteristics under one sun illumination. The power conversion efficiency (PCE) values from IV measurement and EQE corrected are shown in bold.

Sample	Thermal treatment	Jsc (mA/cm^2)	Jsc _EQE (mA/cm^2)	Voc (mV)	FF (%)	PCE (%)	PCE_EQE (%)	Rs (Ω)	Rp (Ω)	P J_{SC}	P MPP
P3HT-I	Non	1.13	1.10	718	28	**0.23**	**0.22**	380	1649	0.34	0.17
P3HT-I	Pre	5.23	4.50	437	57	**1.31**	**1.12**	12	1959	0.81	0.65
P3HT-I	Post	5.88	5.16	642	63	**2.36**	**2.09**	7	3236	0.85	0.71
P3HT-II	Non	4.31	5.66	635	34	**0.92**	**1.22**	52	644	0.55	0.31
P3HT-II	Pre	10.02	8.35	431	52	**2.27**	**1.87**	12	1340	0.89	0.71
P3HT-II	Post	10.53	8.87	602	66	**4.18**	**3.53**	7	4258	0.91	0.80

The photocurrent (J_{ph}) density as a function of effective voltage (V_{eff}) for all devices was calculated and plotted in Fig. 10 in the Appendix on a double logarithmic scale. According to the procedure shown in the in the Appendix, the extraction probability was calculated from the dark and light I–V curves. The values of the extraction probabilities at the J_{SC} and maximum power point (MPP) are shown in Table 1. Annealing significantly improved the extraction probability of charge carriers at short circuit conditions, implying that differences in J_{SC} beyond differences in extraction efficiency must stem from differences in the charge generation efficiency. An extraction barrier is clearly visible in the J–V characteristics of the unannealed device, resulting in low extraction probability at the J_{SC} and MPP. Here, two effects are observed: (i) the extraction probabilities of devices prepared with P3HT-II are significantly higher than those of P3HT-I devices. The P3HT-I-based devices show a distinct extraction barrier. The most likely reason is small and disconnected donor and acceptor phases, which might trap charge carriers and result in generally low mobility. (ii) The post-annealed devices show comparably higher extraction probability, in fact, the highest of all devices at the J_{SC} and MPP. This can be explained by P3HT being phase-separated during annealing and reordered upon cooling at the top electrode.

The absorption spectrum of the photoactive layer is crucial for device performance since it limits the maximum obtainable J_{SC}. Reflectance and transmittance measurements were performed on pristine and blend films, and the absorptance was calculated, as shown in Fig. 3(a) (top: pristine and bottom: blend). From the spectra, two phenomena are clearly observed as a result of thermal annealing: both P3HT samples exhibit a redshift of the absorption peak and an increase in the absorptance. In addition to the redshift of the spectra, an increased crystallinity can be observed indicated by the formation of an additional shoulder at the absorption edge. The red-shifted absorption is an indication of a longer conjugation length of polymer chains in crystalline regions. The absorption spectrum of the annealed films showed two additional peaks at 540 and 600 nm, respectively. This indicates the enhanced crystallinity of the P3HT in the blend after thermal annealing. This is further supported by the PL spectra of the film shown in Fig. 3(b); here, a higher PL intensity was observed for the annealed films. This is a consequence of the larger domain size caused by annealing, supporting the conclusions from the I–V measurements that the domain size of P3HT and PCBM domains are increased. As expected from

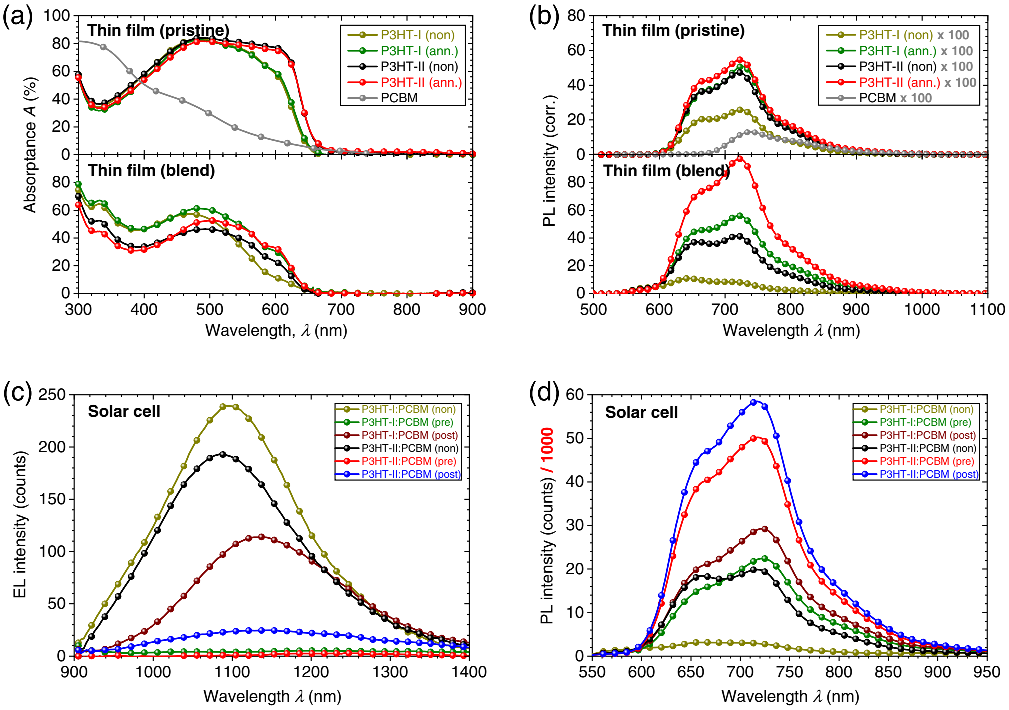

Fig. 3 (a) Absorptance and (b) PL spectra of non-annealed pristine (top) and annealed P3HT:PCBM blend (bottom) films. (c) EL and (d) PL spectra of non-annealed, pre-annealed, and post-annealed P3HT:PCBM solar cells.

PL spectroscopy, the non-annealed films showed a reduced PL signal due to a more intimate mixing, resulting in enhanced PL quenching. The decreased vibronic transition at around 640 nm observed upon annealing indicates the H-aggregate-like crystalline structure of P3HT.[50] The second and third transitions at about 730 and 810 nm, respectively, originate from the H-aggregates of P3HT; however, also PCBM aggregates emit in the same spectral range.

EL spectra of P3HT:PCBM-based solar cells were obtained to identify the CT-state emission from devices. The CT-state emission for such devices is observed in the range of 900 to 1200 nm. Notably, the non-annealed P3HT-I:PCBM device showed EL spectra at a longer wavelength than the non-annealed P3HT-II:PCBM-based device, spectra shown in Fig. 3(c). Although pre-annealed samples show very weak or almost no EL signals, non-annealed devices of both P3HTs showed the highest EL signal, whereas the signals for post-annealed samples are between non-annealed and pre-annealed samples. These differences can be attributed to the annealing conditions of the samples. To gain more insight into the structural changes and the crystallinity of the photoactive layer, SSPL measurements were done on the same devices, shown in Fig. 3(d). As expected, the P3HT-II:PCBM-based device shows higher PL intensity than the P3HT-I:PCBM-based device. In both cases, post-annealed devices show higher PL intensity due to the extensive phase separation, as established by the growing size of PCBM aggregates. The physical changes that occur in the film due to the thermal annealing process ultimately affect the device performance. It is crucial to understand how structural changes are linked to changes in photovoltaic performance.

In order to investigate the exciton quenching efficiency, we performed TRPL measurements following optical excitation at 450 nm of all pristine and photoactive blend thin films on quartz substrates. The TRPL data is presented in Figs. 11 and 12 in the Appendix, showing the spectra at selected time delays with the characteristic PL peak of P3HT at 640 nm. All transients are tracked at 640 nm and shown in Fig. 4. In addition, the data were parameterized using a double exponential decay function, and the weighted-average PL lifetimes were determined, values given in Table 3 in the Appendix. We estimated the PL quenching efficiency using the following

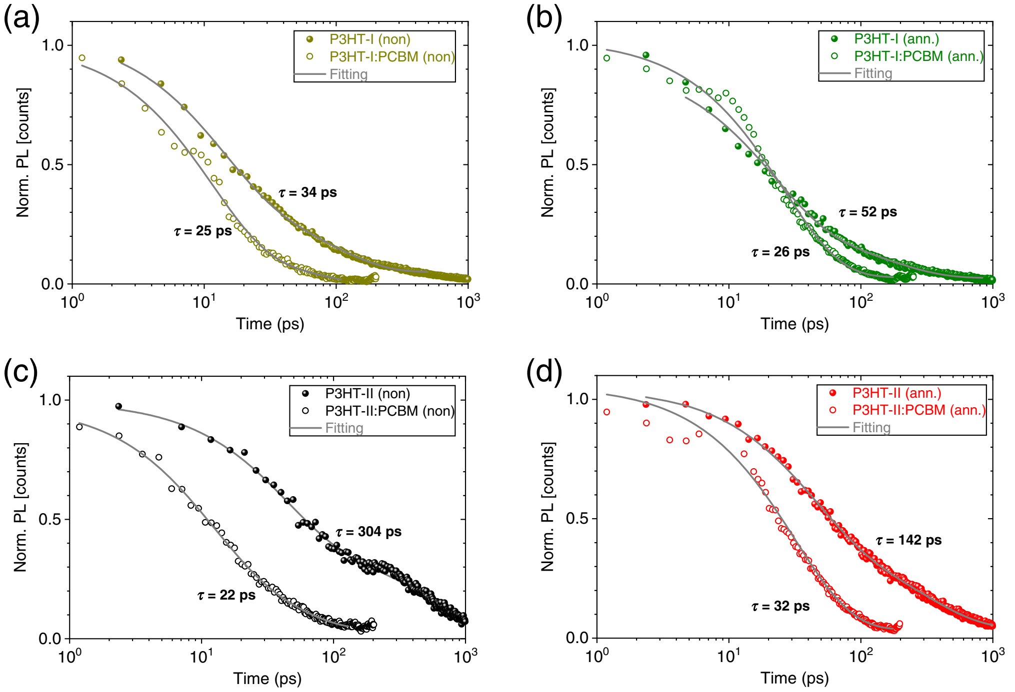

Fig. 4 TRPL transients tracked at the emission of P3HT after optical excitation at 450 nm of both neat donors and the associated photoactive blends. In (a) non-annealed pristine P3HT-I and P3HT-I:PCBM blend data with the fits (solid gray line), (b) annealed pristine P3HT-I and P3HT-I:PCBM blend data, (c) non-annealed pristine P3HT-II and P3HT-II:PCBM blend, and (d) annealed pristine P3HT-II and P3HT-II:PCBM blend.

relation: $1 - t_{\text{blend}}/t_{\text{pristine}}$, where t_{blend} and t_{pristine} are the associated weighted-average PL lifetimes of blend and pristine thin films. We infer that the non-annealed P3HT-II:PCBM yields a close-to-complete PL quenching (93%).

In contrast, the non-annealed P3HT-I:PCBM exhibited an incomplete PL quenching of about 26% (Table 2). In particular, P3HT-II:PCBM blends exhibit improved quenching efficiency, which largely explains the higher photocurrent achieved in solar cells. This is indicative of an improved exciton to charge transfer (CT) state conversion efficiency and potentially higher charge generation yield in P3HT-II-based devices. However, it is worth mentioning that we observe lower PL quenching efficiency (78%) in the annealed P3HT-II:PCBM compared to non-annealed P3HT-II:PCBM-based blends. This supports a coarsening of the photoactive layer morphology in case of the annealed P3HT-II:PCBM devices, which is the reason for the improved transport characteristics and, therefore, the improved photovoltaic parameters.

Furthermore, we conducted AFM on the films used for optical characterization to gain further insight into morphological changes. Figure 5 shows the height images of non-annealed and annealed pristine P3HT-(I&II) and P3HT-(I&II):PCBM blend films. Pristine P3HT-I material shows higher surface roughness and larger feature sizes than the blend using the same polymer. Interestingly, P3HT-II exhibited more significant features than P3HT-I, which can be explained by its enhanced crystallinity. Thermal annealing of pristine P3HT films did not result in any apparent changes, while thermal annealing of the blends clearly caused a higher surface roughness. The images confirm the increased crystallinity of P3HT, which enhances the charge transport properties in devices. These differences can also explain why the pre-annealed samples generally show less improved series resistance than the post-annealed ones. Due to the annealing without a constraining layer, the film coarseness increases, resulting in a worse contact between the electrode and the active layer. Upon post-annealing, the surface structure of the film is mainly conserved, as there is a solid layer on top of the active layer, constraining the vertical direction.

To connect the morphological differences observed upon annealing of the film with EL spectra of the solar cells, ELI of cells prepared by different processing conditions was done, results are shown in Fig. 6. ELI is very sensitive to the device series resistance, though this series resistance itself is a composite value itself. It is consisting of the sheet resistances of the electrodes, the contact resistance between all the layers, and the series resistance of the charge transport layers and the photoactive layer. In addition to the defects, non-annealed samples show a lateral rather than homogeneous emission. This is in agreement with the high series resistance of the device photoactive layer, which makes any impact of the series resistance from the ITO negligible. The emission perceived stems from a single spot that is heated due to the high resistance of the surrounding layer and the resulting current flow through a small area. Furthermore, the non-annealed samples show an inhomogeneous emission, the overall shape of the emission is not dominated by the usual current crowding pattern seen in the post-annealed devices. The current crowding stems from the difference in resistance for the ITO and Al electrodes, where the Al electrode shows a significantly lower resistance than the ITO electrode, resulting in the current flowing for as long as possible along the Al electrode and preferentially passing through the HTL and active layer close to the extracting contact into the ITO. As such a pattern is not visible in the non-annealed sample, this means that the annealing itself results also in a homogenization of the active layer resistance and/or the contact resistances of the active layer.

Table 2 PL quenching efficiency determined from TRPL measurements.

Sample	Treatment	TRPL quenching efficiency
P3HT-I:PCBM	Non-annealed	26
P3HT-I:PCBM	Annealed	50
P3HT-II:PCBM	Non-annealed	93
P3HT-II:PCBM	Annealed	78

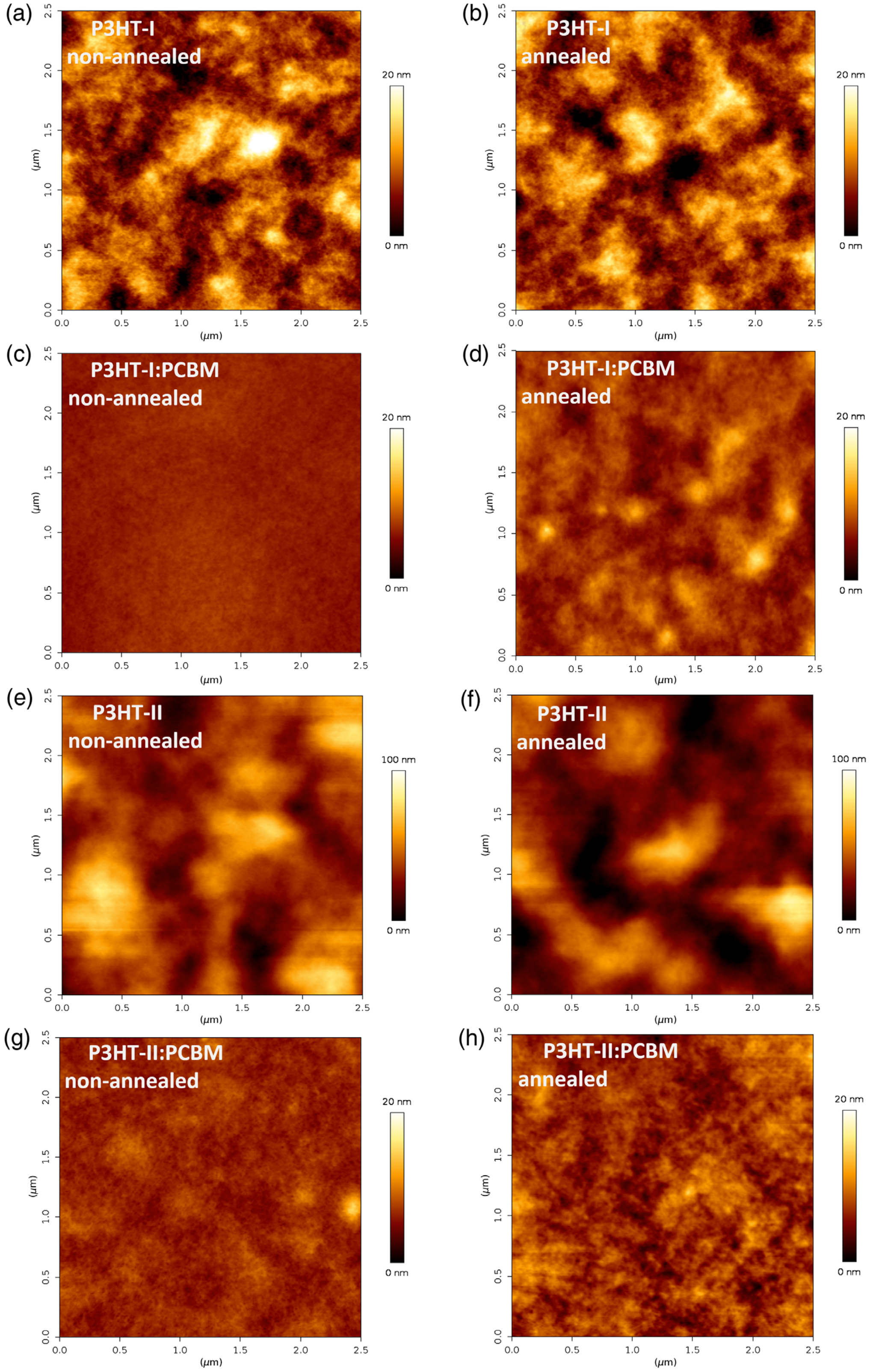

Fig. 5 AFM height images of P3HT-(I&II):PCBM as cast and annealed films. (a) P3HT-I (non-annealed); (b) P3HT-I (annealed); (c) P3HT-I:PCBM (non-annealed), (d) P3HT-I:PCBM (annealed); (e) P3HT-II (non-annealed); (f) P3HT-II (annealed); (g) P3HT-I:PCBM (non-annealed); and (h) P3HT-II:PCBM (annealed).

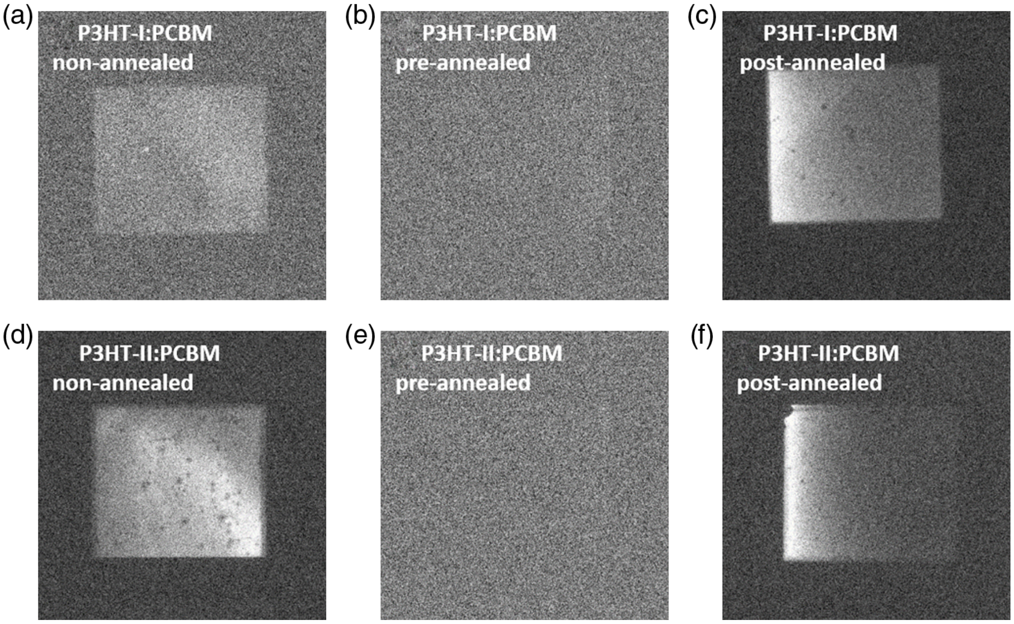

Fig. 6 ELI for the P3HT:PCBM solar cells. (a) P3HT-I:PCBM (non-annealed); (b) P3HT-I:PCBM (pre-annealed); (c) P3HT-I:PCBM (post-annealed); (d) P3HT-II:PCBM (non-annealed); (e) P3HT-II:PCBM (pre-annealed); and (f) P3HT-II:PCBM (post-annealed).

Figures 6(b) and 6(e) show the cell annealed before anode deposition; there is only a very faint signal visible of one of the device's edges. This suggests some current crowding occurs, i.e., the current distribution across the device is determined by the electrode resistances, but the series resistance of the active layer and/or its contact resistances is very high. Though the aforementioned resistances are very high, they seem to be still homogeneous as the weak visible signal only indicates current crowding based on the electrode resistances is occurring, i.e., also for the pre-annealed samples, the annealing process is homogenizing the resistances of the active layer.

Both of the post-annealed samples showed the phenomenon of current crowding; the reason is the series resistance of the ITO, which results in carriers following the shortest path through the ITO. Furthermore, some current crowding is also visible on the edge closest to the negative contact of the cell layout. This is due to the different conductivity of two different electrodes, namely, ITO and aluminum. Additionally, some dark spots can be seen from the sample on the top of the image, and these dark spots stem from local areas of increased series resistance and might be connected to either local blocking contacts or undissolved materials.

4 Summary

To summarize, the main aspects that affect the performance of P3HT:PCBM OSCs prepared with different annealing conditions have been discussed. The nanoscale morphology of the donor–acceptor phase in a BHJ plays a vital role in determining the efficiency of the device. The analysis shows that the post-annealing step led to significantly improved device performance in the case of P3HT-II, as in this case, the active layer is already constrained in two dimensions by a material with different surface energy than the air on top of it, and this changes the way the morphology is altered upon annealing. First, it seems that during pre-annealing, when N_2 (glovebox environment) is on top of the film, the P3HT preferentially phase separates toward the surface, while when Al is on top, as under post-annealing, PCBM seems to preferentially diffuse to the top, as can be seen from the enormously improved series resistance of the post-annealed devices. A schematic of the ordering of the P3HT:PCBM devices upon annealing sequences and their morphological changes are shown in Fig. 7.

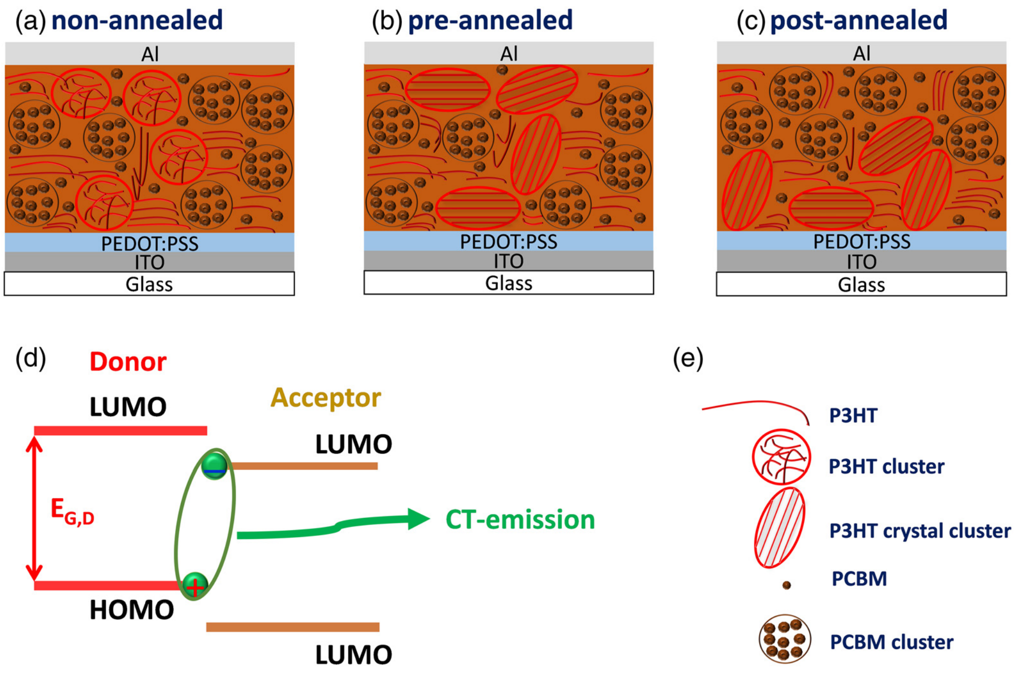

Fig. 7 Schematic of the ordering the P3HT:PCBM devices, (a) non-annealed; (b) pre-annealed; (c) post-annealed; (d) energy levels of donor-acceptor interface; and (e) P3HT crystals and PCBM cluster.

Furthermore, the charge carriers recombine non-radiatively *via* trap/defect states, P3HT: PCBM films might unintentionally be doped by impurities while annealing the neat films in the glovebox. Second, this constraint due to the electrode also hinders the film to develop columnar structures and a rougher surface. Therefore, a good contact remains, but in this case, an improved active layer morphology also allows for higher conductivity through mutually connected phases. The annealing prior to deposition of the top electrode resulted in a less favourable morphology than the post-annealed device due to the released heat upon annealing without the top electrode. Besides, a very thin P3HT layer might grow laterally during thermal treatment in the absence of an Al electrode and perform as a barrier for electron transport from the P3HT: PCBM matrix to the cathode.[51]

In the case of the post-annealed sample, the Al electrode fully covers the photoactive layer, and thus the photoactive layer has only limited space. Consequently, molecules cannot move over the entire substrate resulting in a very ordered structure of the P3HT:PCBM network formed upon cooling. Furthermore, Al interdiffusion that happened due to the annealing process hinders the alignments of P3HT crystals from the surface's normal direction and lowers the contact resistance between the Al electrode and the P3HT:PCBM layer. Another significant factor is the orientational distribution of the P3HT crystals while annealing the sample with the presence of an Al layer on top of the P3HT:PCBM layer decreases the favored orientation and total crystallinity of the P3HT crystals, supporting the formation of the interpenetrating networks and thus face-on P3HT crystals preferably regioregular P3HT (P3HT-II) in the surface region affect device performance.[52,53] However, due to the vertical phase separation and improvement in crystallinity of P3HT and PCBM for the pre-annealed device, charge carriers are being separated from each other. As a result, the CT-state emission for those devices is poorly visible, and excitons convert to CT states efficiently, while charges are not separate due to the barrier.

5 Conclusion

We presented an extensive study on P3HT:PCBM-based OSCs from a didactic perspective. We found that different thermal treatment conditions improve the performance of OSCs based on the active layer blend of P3HT:PCBM. It is thereby significant to mention that when the devices are thermally treated (before and after electrode deposition), it shows the highest effect after electrode deposition, most likely due to the constraints set to diffusion through the additional adjacent layer. This reduces the available degrees of freedom for the reorganization of the materials in the blend. Furthermore, it changes the surface energy at the top of the film, resulting in a more favorable stratification of the active layer upon annealing after electrode deposition. In this case, charge carriers can still recombine non-radiatively, as confirmed by EL emission and EL imaging measurements, where very moderate or almost no signals were detected. Morphological structure and photoluminescence studies demonstrated the highest film crystallinity for annealed films, which is responsible for the improved photovoltaic characteristics upon annealing. The overall performance of the post-annealed devices is higher than the as-cast and pre-annealed devices, which suggests that the sequence of the processing steps is essential, and the device post-annealing is essential to obtain efficient charge carrier collection.

6 Appendix

6.1 *Step-by-Step Process of Device Preparation*

The step-by-step device preparation process is shown in part I of Fig. 8. In part II of Fig. 8, three annealing conditions for the active layer films are shown with some schematics.

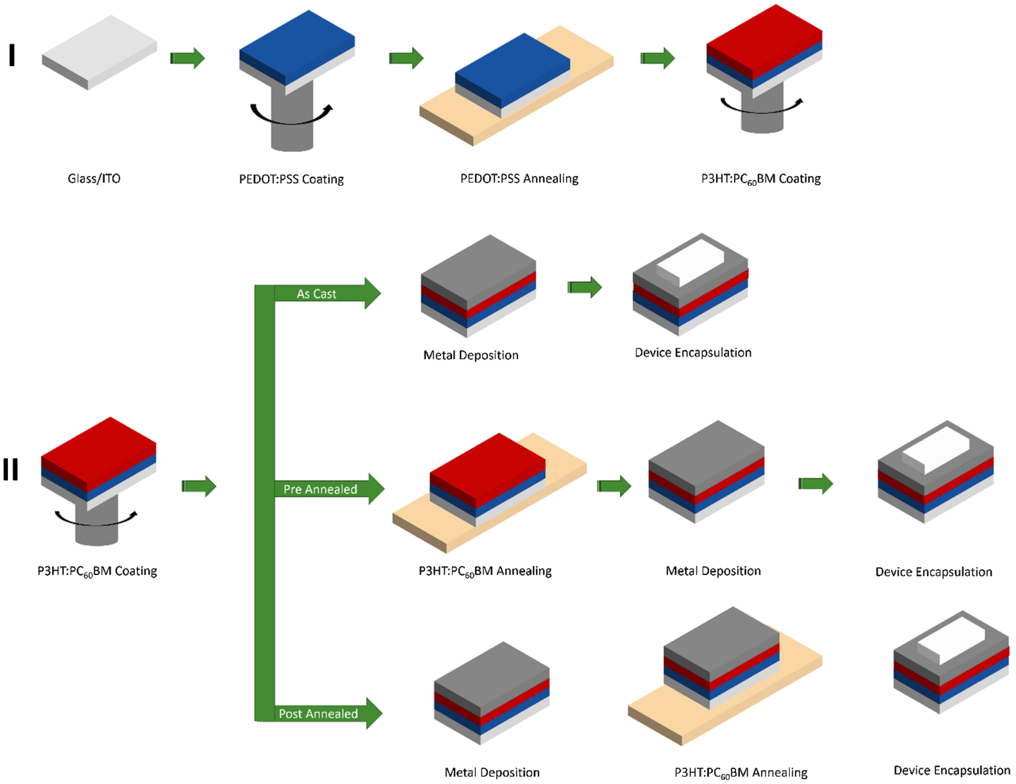

Fig. 8 Schematic diagram for the step-by-step process of P3HT:PCBM-based thin-film OSCs (i), annealing treatment on the active layer films in different conditions (ii).

6.2 *Statistical Evaluation of I–V Measurements*

In order to look at the reproducibility of device preparation statistical evaluation of all the solar cells is shown in the section. The average value and standard deviation of all photovoltaics parameters are shown in the graph. The averages were calculated from 8 solar cell devices prepared for the same experiment (Figs. 9 and 10).

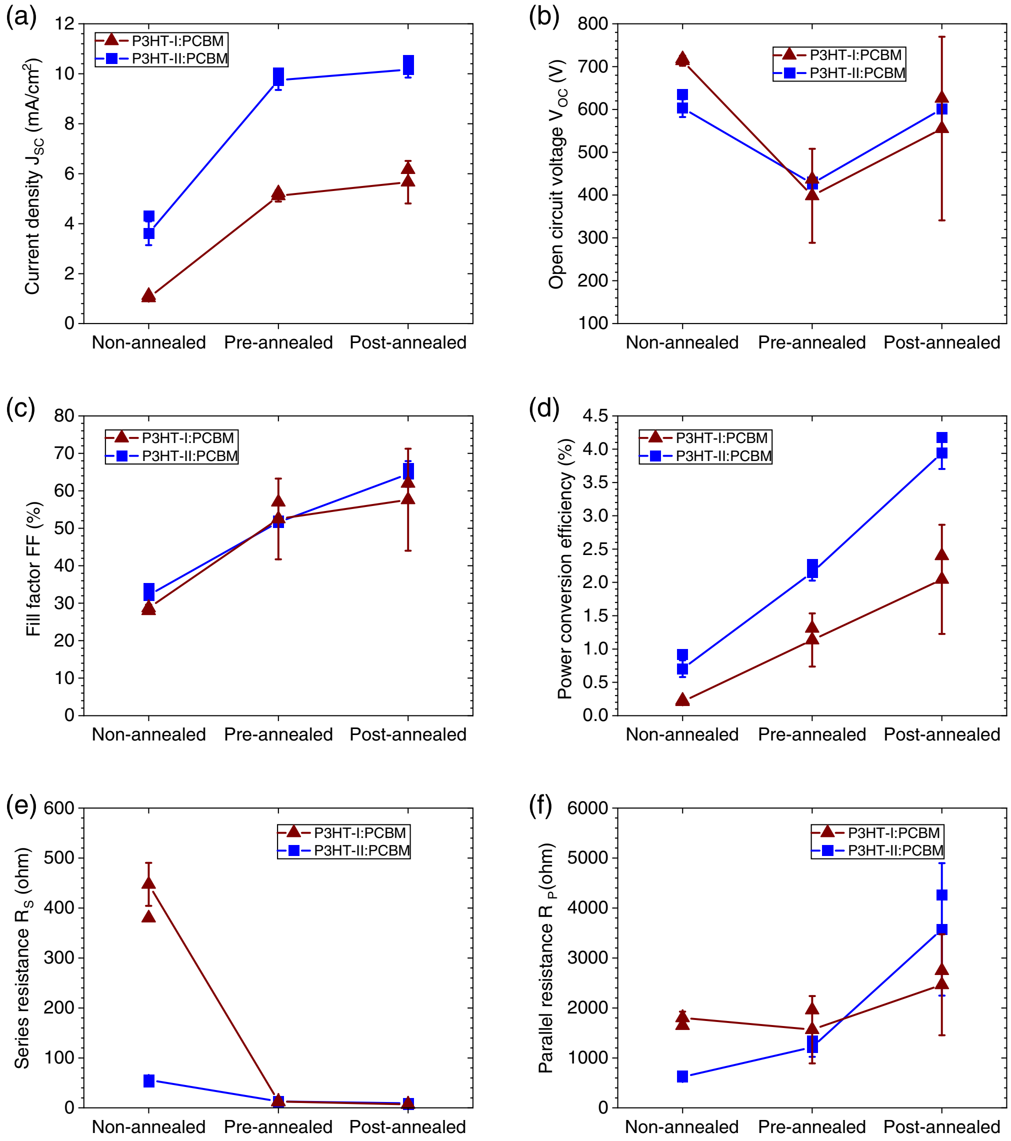

Fig. 9 Statistical evaluations of photovoltaic parameters (J_{sc}, V_{oc}, FF, PCE, R_s, and R_p) of P3HT:PCBM devices in conventional architecture. The parameters are plotted versus the pre and post-annealed sample and compared to as-cast samples.

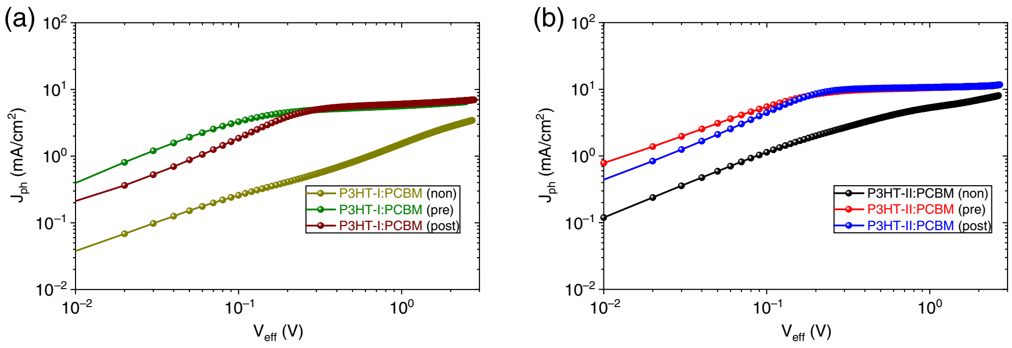

Fig. 10 Photo-current density (J_{ph}) as a function of the effective voltage (V_{eff}) for thermally treated P3HT:PCBM solar cells upon different annealing conditions (non-annealed, pre-annealed, post-annealed). (a) P3HT-I:PCBM and (b) P3HT-II:PCBM.

6.3 *Extraction Probability*

The extraction probability was calculated from the dark and light I–V curves according to the following procedure.

First, the photo-current density was calculated as follows:

$$J_{\text{ph}} = J_L - J_D,$$

with J_L being the light current density and J_D being the dark current density.

Then, we determined the built-in potential V_{bi}, which is equal to the voltage at zero current photo density $(V_{\text{bi}} = V(J_{\text{ph}} = 0))$.

From this, we then calculated the potential across the solar cell:

$$V = V_{bi} - V_{\text{appl}},$$

with V_{appl} being the externally applied voltage over the solar cell.

Finally, to calculate the extraction efficiencies at short circuit current density $(P_{J_{\text{SC}}})$ and MPP (P_{MPP}) we calculated the ratio between the $J_{\text{ph}}(V_{\text{appl}} = 0)$ to J_{ph} at saturation or respectively, $J_{\text{ph}}(V_{\text{appl}} = V_{\text{MPP}})$.

6.4 *Time-Resolved Photoluminescence*

The TRPL spectra at selected time delays with characteristics PL peaks are shown in this section (Figs. 11 and 12). The data were parameterized using a double exponential decay function and the weighted-average PL lifetimes were determined; the values are shown in Table 3.

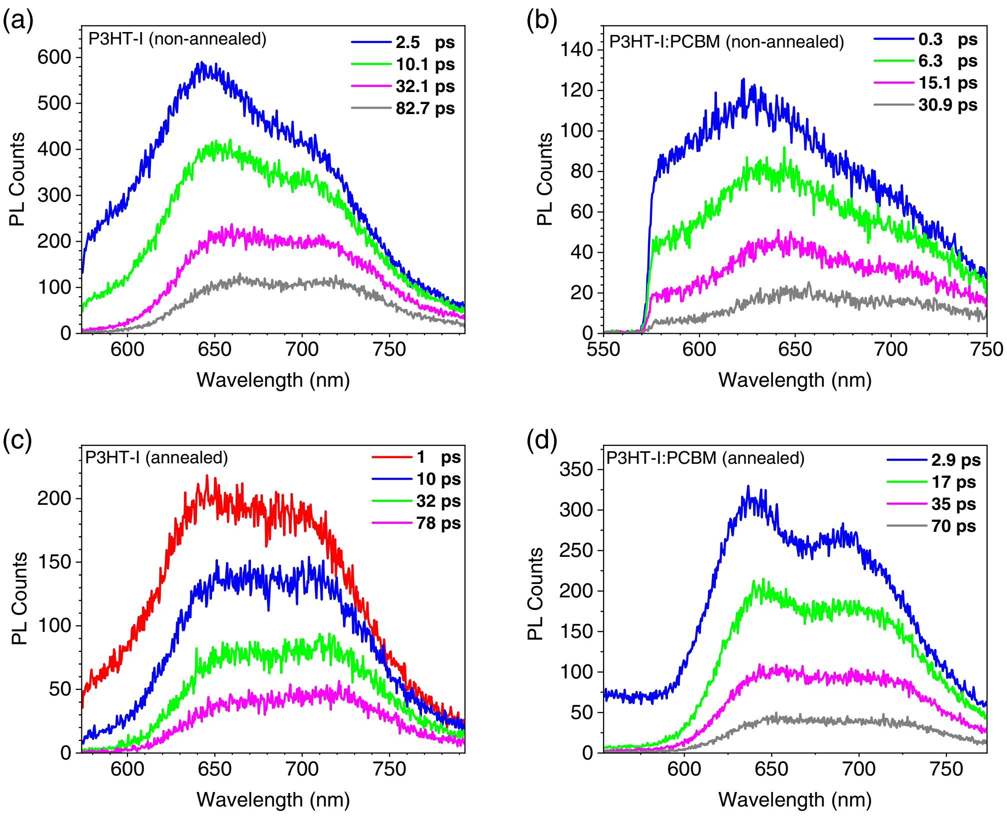

Fig. 11 Time-resolved PL spectra of (a) P3HT-I (non-annealed); (b) P3HT-I:PCBM (non-annealed); (c) P3HT-I (annealed); and (d) P3HT-I:PCBM (annealed).

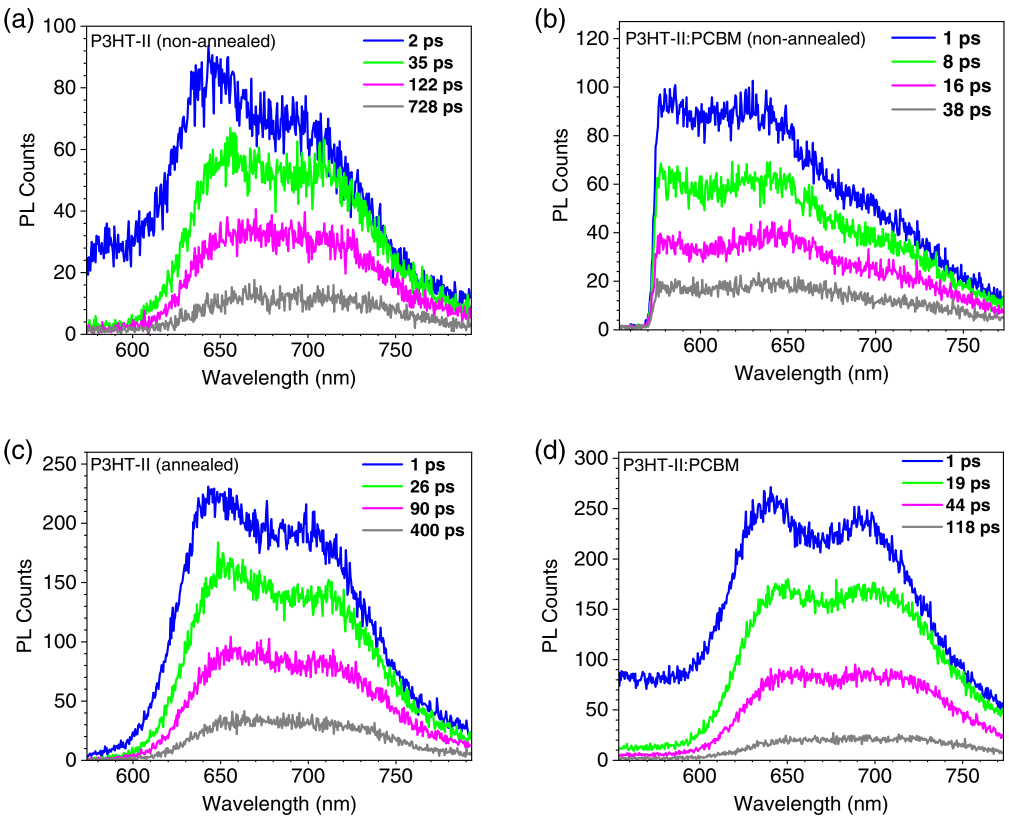

Fig. 12 TRPL spectra of (a) P3HT-II (non-annealed); (b) P3HT-II:PCBM (non-annealed); (c) P3HT-II (annealed); and (d) P3HT-II:PCBM (annealed).

Table 3 Parametrized time constants t_1 and t_2 extracted from double exponential fits to the respective decays and extracted weighted-averaged $\tau_{\text{avg,wt}}$ lifetimes.

	A_1	A_2	t_1 (ps)	t_2 (ps)	$\tau_{\text{avg,wt}}$ (ps)
P3HT-I	0.68	0.22	21	153	52
P3HTI:PCBM (ann)	0.99	—	26	—	26
P3HT-II	0.63	0.38	41	306	142
P3HTII:PCBM (ann)	0.52	0.50	32	32	32
P3HT-I	0.90	0.14	11	109	34
P3HTI:PCBM (non-ann)	0.67	0.33	13	88	25
P3HT-II	0.60	0.42	42.2	719.8	304
P3HTII:PCBM (non-ann)	0.61	0.33	10.3	42.2	22

Acknowledgments

SA and HH are grateful for financial support from Deutsche Forschungsgemeinschaft (DFG) in the frame of "PhotoGenOrder" project. This work was supported by the King Abdullah University of Science and Technology (KAUST) Office of Sponsored Research (OSR) under Award No. OSR-2018-CARF/CCF-3079. The authors appreciate for atomic force microscopy measurements supported by Susanne Sandkuhl at the FSU Jena.

References

1. L. X. Chen, “Organic solar cells: recent progress and challenges,” *ACS Energy Lett.* **4**(10), 2537–2539 (2019).
2. W. Liu et al., “Low-bandgap non-fullerene acceptors enabling high-performance organic solar cells,” *ACS Energy Lett.* **6**(2), 598–608 (2021).
3. C. Yan et al., “Non-fullerene acceptors for organic solar cells,” *Nat. Rev. Mater.* **3**(3), 18003 (2018).
4. S. R. Gollu et al., “Thermal annealing study on P3HT: PCBM based bulk heterojunction organic solar cells using impedance spectroscopy,” in *Light and Its Interactions with Matter*, P. Predeep and A. Sujith, eds., Vol. **1620**, pp. 150–156, American Institute of Physics, Melville (2014).
5. H. Hoppe and N. S. Sariciftci, “Organic solar cells: an overview,” *J. Mater. Res.* **19**(7), 1924–1945 (2004).
6. R. C. I. MacKenzie et al., “Modeling nongeminate recombination in P3HT:PCBM solar cells,” *J. Phys. Chem. C* **115**(19), 9806–9813 (2011).
7. F. Liu et al., “Molecular weight dependence of the morphology in P3HT:PCBM solar cells,” *ACS Appl. Mater. Interfaces* **6**(22), 19876–19887 (2014).
8. B. T. de Villers et al., “Improving the reproducibility of P3HT:PCBM solar cells by controlling the PCBM/cathode interface,” *J. Phys. Chem. C* **113**(44), 18978–18982 (2009).
9. J. C. Byers et al., “Mechanism of recombination losses in bulk heterojunction P3HT: PCBM solar cells studied using intensity modulated photocurrent spectroscopy,” *ACS Appl. Mater. Interfaces* **3**(2), 392–401 (2011).
10. M. T. Dang, L. Hirsch, and G. Wantz, “P3HT:PCBM, best seller in polymer photovoltaic research,” *Adv. Mater.* **23**(31), 3597–3602 (2011).
11. J. N. Burghartz, “Introduction to organic electronics,” in *Short-Channel Organic Thin-Film Transistors: Fabrication, Characterization, Modeling and Circuit Demonstration*, pp. 5–31, Springer-Verlag, Berlin (2015).
12. S. R. Forrest and M. E. Thompson, “Introduction: organic electronics and optoelectronics,” *Chem. Rev.* **107**(4), 923–925 (2007).
13. J. M. Shaw and P. F. Seidler, “Organic electronics: introduction,” *IBM J. Res. Dev.* **45**(1), 3–9 (2001).
14. A. T. Kleinschmidt, S. E. Root, and D. J. Lipomi, “Poly(3-hexylthiophene) (P3HT): fruit fly or outlier in organic solar cell research?” *J. Mater. Chem. A* **5**(23), 11396–11400 (2017).
15. M. Van Landeghem et al., “Disentangling overlapping high-field EPR spectra of organic radicals: Identification of light-induced polarons in the record fullerene-free solar cell blend PBDB-T:ITIC,” *J. Magn. Reson.* **288**, 1–10 (2018).
16. Z. Li et al., “Effects of 1,8-diiodooctane on ultrafast charge carrier dynamics and photovoltaic performance in organic solar cells: a comparison of $PC_{71}BM$ and nonfullerene acceptor IT-M,” *Organic Electron.* **81**, 105690 (2020).
17. W. C. Zhao et al., “Fullerene-free polymer solar cells with over 11% efficiency and excellent thermal stability,” *Adv. Mater.* **28**(23), 4734–4739 (2016).
18. T. R. Andersen et al., “Novel cost-effective acceptor: P3HT based organic solar cells exhibiting the highest ever reported industrial readiness factor,” *Mater. Adv.* **1**(4), 658–665 (2020).
19. L. J. A. Koster, V. D. Mihailetchi, and P. W. M. Blom, “Bimolecular recombination in polymer/fullerene bulk heterojunction solar cells,” *Appl. Phys. Lett.* **88** (5), 052104 (2006).
20. D. Kim et al., “Heterogeneous interfacial properties of ink-jet-printed silver nanoparticulate electrode and organic semiconductor,” *Adv. Mater.* **20**(16), 3084–3089 (2008).
21. C. E. Cheng et al., “Influences of thermal annealing on P3HT/PCBM interfacial properties and charge dynamics in polymer solar cells,” *Jpn. J. Appl. Phys.* **54**(12), 122301 (2015).
22. E. Verploegen et al., “Effects of thermal annealing upon the morphology of polymer-fullerene blends,” *Adv. Funct. Mater.* **20**(20), 3519–3529 (2010).
23. I. Singh et al., “Effect of thermal annealing on the efficiency of poly (3-hexylthiphone): 6,6 - phenyl-C_{61}-butyric acid methyl ester bulk heterojunction solar cells,” *J. Nanophotonics* **5**, 3504 (2011).

24. O. Oklobia and T. S. Shafai, “A study of donor/acceptor interfaces in a blend of P3HT/PCBM solar cell: effects of annealing and PCBM loading on optical and electrical properties,” *Solid-State Electron.* **87**, 64–68 (2013).
25. F. Padinger, R. S. Rittberger, and N. S. Sariciftci, “Effects of postproduction treatment on plastic solar cells,” *Adv. Funct. Mater.* **13**(1), 85–88 (2003).
26. J. F. Chang et al., “Enhanced mobility of poly(3-hexylthiophene) transistors by spin-coating from high-boiling-point solvents,” *Chem. Mater.* **16**(23), 4772–4776 (2004).
27. Y. T. Wang et al., “Use of ultrafast time-resolved spectroscopy to demonstrate the effect of annealing on the performance of P3HT:PCBM solar cells,” *ACS Appl. Mater. Interfaces* **7**(8), 4457–4462 (2015).
28. J. Bisquert and G. Garcia-Belmonte, “On voltage, photovoltage, and photocurrent in bulk heterojunction organic solar cells,” *J. Phys. Chem. Lett.* **2**(15), 1950–1964 (2011).
29. G. F. Burkhard et al., “Free carrier generation in fullerene acceptors and its effect on polymer photovoltaics,” *J. Phys. Chem. C* **116**(50), 26674–26678 (2012).
30. G. F. A. Dibb et al., “Analysis of the relationship between linearity of corrected photocurrent and the order of recombination in organic solar cells,” *J. Phys. Chem. Lett.* **2**(19), 2407–2411 (2011).
31. O. P. Dimitriev et al., “Effect of the polymer chain arrangement on exciton and polaron dynamics in P3HT and P3HT:PCBM films,” *J. Phys. Chem. C* **122**(30), 17096–17109 (2018).
32. C. Kastner et al., “Revelation of interfacial energetics in organic multiheterojunctions,” *Adv. Sci.* **4**(4), 1600331 (2017).
33. D. M. Gonzalez et al., “Codependence between crystalline and photovoltage evolutions in P3HT:PCBM solar cells probed with in-Operando GIWAXS,” *ACS Appl. Mater. Interfaces* **9**(4), 3282–3287 (2017).
34. W. C. Tsoi et al., “Effect of crystallization on the electronic energy levels and thin film morphology of P3HT:PCBM blends,” *Macromolecules* **44**(8), 2944–2952 (2011).
35. S. Alam et al., “High-temperature stable single carrier hole only device based on conjugated polymers,” *J. Mater. Res.* **33**(13), 1860–1867 (2018).
36. C. R. Singh et al., “Correlation of charge transport with structural order in highly ordered melt-crystallized poly(3-hexylthiophene) thin films,” *J. Polym. Sci. Pt. B-Polym. Phys.* **51**(12), 943–951 (2013).
37. W. C. Huang et al., “In-depth understanding of the morphology-performance relationship in polymer solar cells,” *ACS Appl. Mater. Interfaces* **7**(25), 14026–14034 (2015).
38. A. Singh et al., “Effect of dual cathode buffer layer on the charge carrier dynamics of rrP3HT:PCBM based bulk heterojunction solar cell,” *ACS Appl. Mater. Interfaces* **8**(17), 10904–10910 (2016).
39. R. C. I. MacKenzie et al., “Interpreting the density of states extracted from organic solar cells using transient photocurrent measurements,” *J. Phys. Chem. C* **117**(24), 12407–12414 (2013).
40. J. A. Reinspach et al., “Tuning the morphology of solution-sheared P3HT:PCBM films,” *ACS Appl. Mater. Interfaces* **8**(3), 1742–1751 (2016).
41. W. J. Wang et al., “Development of the morphology during functional stack build-up of P3HT:PCBM Bulk heterojunction solar cells with inverted geometry,” *ACS Appl. Mater. Interfaces* **7**(1), 602–610 (2015).
42. S. Lilliu et al., “Dynamics of crystallization and disorder during annealing of P3HT/PCBM bulk heterojunctions,” *Macromolecules* **44**(8), 2725–2734 (2011).
43. Q. Wu, M. Bhattacharya, and S. E. Morgan, “POSS-enhanced phase separation in air-processed P3HT:PCBM bulk heterojunction photovoltaic systems,” *ACS Appl. Mater. Interfaces* **5**(13), 6136–6146 (2013).
44. B. F. Xue et al., “Vertical stratification and interfacial structure in P3HT:PCBM organic solar cells,” *J. Phys. Chem. C* **114**(37), 15797–15805 (2010).
45. A. L. Ayzner et al., “Room to improve conjugated polymer-based solar cells: understanding how thermal annealing affects the fullerene component of a bulk heterojunction photovoltaic device,” *J. Phys. Chem. C* **112**(48), 18711–18716 (2008).
46. A. Ng et al., “Annealing of P3HT:PCBM blend film-the effect on its optical properties,” *ACS Appl. Mater. Interfaces* **5**(10), 4247–4259 (2013).

47. H. Wang et al., “Exciton diffusion and charge transfer dynamics in nano phase-separated P3HT/PCBM blend films,” *Nanoscale* **3**(5), 2280–2285 (2011).
48. T. Erb et al., “Correlation between structural and optical properties of composite polymer/fullerene films for organic solar cells,” *Adv. Funct. Mater.* **15**(7), 1193–1196 (2005).
49. I. A. Howard et al., “Effect of morphology on ultrafast free carrier generation in polythiophene: fullerene organic solar cells,” *J. Am. Chem. Soc.* **132**(42), 14866–14876 (2010).
50. F. C. Spano and C. Silva, “H- and J-aggregate behavior in polymeric semiconductors,” *Annu. Rev. Phys. Chem.* **65**, 477–500 (2014).
51. H. J. Kim et al., “The effect of Al electrodes on the nanostructure of poly(3-hexylthiophene): fullerene solar cell blends during thermal annealing,” *Organic Electron.* **10**(8), 1505–1510 (2009).
52. H. J. Kim, H. H. Lee, and J. J. Kim, “Real time investigation of the interface between a P3HT:PCBM layer and an al electrode during thermal annealing,” *Macromol. Rapid Commun.* **30**(14), 1269–73 (2009).
53. H. J. Kim, J. W. Kim, and J. -J. Kim, “Invited paper: nanostructures of a mixed donor and acceptor layer in organic photovoltaics,” *Electron. Mater. Lett.* **7**(2), 93–104 (2011).

Shahidul Alam is a postdoctoral fellow at King Abdullah University of Science and Technology (KAUST), KAUST Solar Center, Saudi Arabia. He received his BSc degree in physics from Bangladesh and MSc degree in electronics engineering, Germany. In 2020, he obtained PhD in physical chemistry from Friedrich Schiller University Jena, Germany. His current research interests include charge transport in organic semiconductors, crystallinity, structure-property relation, device performance, and stability of solution-processed polymer solar cells.

Biographies of the other authors are not available.